Flash Spark Plasma Sintering of 3YSZ: Modified sintering pathway and impact on grain boundary formation

Thomas Hérisson de Beauvoir, Zakaria Ghomari, Geoffroy Chevallier, Andréas Flaureau, Alicia Weibel, Catherine Elissalde, Fabrice Mauvy, Rachman Chaim, Claude Estournès

Flash Spark Plasma Sintering of 3YSZ: Modified sintering pathway and impact on grain boundary formation

Thomas Hérisson de Beauvoir[1], Zakaria Ghomari[1], Geoffroy Chevallier[1], Andréas Flaureau[1], Alicia Weibel[1], Catherine Elissalde[2], Fabrice Mauvy[2], Rachman Chaim[3], Claude Estournès[1]

[1] CIRIMAT, CNRS-INP-UPS, Université Toulouse 3 – Paul Sabatier, 118 route de Narbonne, 31062 Toulouse, France
[2] CNRS, Université de Bordeaux, ICMCB, UMR 5026, 87 Avenue du Dr A. Schweitzer, 33608, Pessac, France
[3] Department of Materials Science and Engineering, Technion – Israel Institute of Technology, Haifa 32000 Israel

Yttria stabilized zirconia (3 mol% YSZ) ceramics were prepared by Flash-SPS, while allowing high heating rates up to 200°C/s, which led to the extremely fast densification within a few seconds. The high heating rates had strong impact on sintering mechanisms, in terms of densification and grain growth. While the specimens ended with 5 to 15 vol% porosity and limited grain growth (< 350 nm), their hardness is higher than fully dense counterpart SPSed ceramics. Using the sintering trajectories, microstructural observations, and impedance spectroscopy, we highlight altered sintering mechanism which resulted in very thin grain boundaries compared to SPS. It appears that densification is largely advanced at grain boundary interfaces, with no residual nano-pores at the grain junctions, where some pores with size comparable to grain size were present. This opens up opportunities for the fabrication of porous lightweight ceramics with good mechanical properties.

1. Introduction

Electric field assisted sintering techniques have attracted a huge interest in the last decade. These allow the application of sintering to a very broad range of ceramics. Spark Plasma Sintering (SPS) technique is the most common field assisted sintering technique, due to its versatility in sintering of different materials, but also size and shape control [1–3]. In addition, SPS technique relies on the application of a uniaxial pressure on the powder compact to enhance grain to grain contact, promote grain rearrangement in the first stage of sintering, and grain

sliding during further steps [4]. While SPS relies on the application of high current density at low electric field, Flash Sintering (FS) consists the application of high electric fields at low current densities on the green powder compact. FS is mostly used for materials exhibiting semi-conducting behavior and is a pressureless sintering technique [5]. Generally, high densification rates can be obtained thanks to the application of the electric field to a pre-heated specimen, leading to an electrical discharge hence extremely fast densification kinetics [6]. The main problems encountered during FS deals with the difficulty to control microstructural homogeneity over the sintered specimens [7]. In order to get benefit from both techniques while avoiding microstructural heterogeneity, the SPS setup was modified to reach heating rates in the same range as in FS [8, 9]. Olevsky *et al.* [8] applied SPS using a modified die setup in which an empty Cu tube was used to avoid initial direct electric contact between the top electrode and the specimen. While the experiment was running, the current passed through the Cu tube resulted in its fast heating hence its plastic deformation. While Cu tube deformed, the top electrode came into contact with the punch, suddenly applying both pressure and electric current to the powder compact. This way, ultra-rapid sintering was imposed on SiC compact while controlling the thermal runaway by application of the uniaxial pressure. They further developed another setup, called net shape Flash SPS [9], to generate very high heating rates just by adding an isolating BN layer between the graphite foil and the die inner surface. This way, the electric current was forced to pass through the specimen or in the thin graphite foil which surrounded it, allowing high heating rate and efficient sintering. This technique was successfully applied to materials with negative temperature coefficient (NTC) behavior of their electric resistivity either ionic conductors (stabilized zirconia) or insulating oxide (Al_2O_3), and to metallic Ni. Similar heating rate effects directly through the specimen were achieved by Grasso and coworkers [10–12] by powder consolidation into a cohesive pellet prior to SPS, after which the pressure and electric current were simultaneously applied to a sample wrapped

in a graphite foil. They successfully densified non-oxide ceramics such as ZrB_2, TiB_2 and SiC. This technique, called Flash SPS (FSPS), has been recently applied for densification of binary ($BaTiO_3$) and ternary ($CaCu_3Ti_4O_{12}$) oxides [13]. The common feature of these setups is the application of a uniaxial pressure while the electric current (under a low voltage, typically < 10 V) is forced to pass across a porous specimen to promote its densification by thermal runaway. Another strategy is by using a classic SPS setup with thinner die, allowing the current to flow both through the die and the specimen, depending on their respective conductivity. Using thinner die leads to an increased current density as compared to classic SPS, eventually leading to fast heating rates. Niu *et al.* [14] applied this technique for fabrication of B_4C. In their setup, the temperature was shown to increase from room temperature to ~ 1900°C in less than 20 seconds, with a 2 mm thick die.

FSPS was also applied to Yttria Stabilized Zirconia [15,16], but evidences of sintering mechanisms and resulting microstructures are still missing. In the present work we applied SPS and FSPS to 3 mol.% yttria stabilized zirconia (3YSZ) to explore the influence of the FSPS process on the microstructural features, through the use of sintering trajectory, and to highlight their relations to the mechanical and electrical properties. In order to achieve very fast heating rates under the applied pressure, a 20 mm inner diameter graphite die was prepared with a die thickness of only 5 mm. Using this setup enables extremely high thermal ramps. The present study focuses on the microstructural evolution through sintering trajectories, and explore the effect of the observed microstructural changes on the mechanical properties. To further support our observations, electrical impedance spectroscopy was used to evaluate both grain and grain boundary contributions, comparing specimens sintered by SPS and Flash-SPS.

2. Experimental

Commercial 3YSZ (Tosoh) powder with nanometric average particle sizes (~ 40 nm) was used for all sintering experiments. SPS experiments were performed using a FUJI 632Lx and Flash-SPS (FSPS) experiments using a Dr. Sinter 2080 (SPS Syntex Inc, Japan) apparati (using pulsed DC sources), both located at the Plateforme Nationale CNRS de Frittage Flash at the University of Toulouse III - Paul Sabatier. Graphite dies (15 and 5 mm thickness for SPS and FSPS, respectively) were used while a 0.2 mm graphite paper was placed all around the specimen in all experiments under primary vacuum (~ 10 Pa). Typical specimen size prepared is 20 mm diameter, with a thickness of 3 mm. Using such setup allows the main current to flow through the die, generating heat. At elevated temperatures, 3YSZ becomes conductive, allowing the current to flow and generate heating from the thermal runaway [9]. In FSPS experiments, a lower pressure of 25 MPa was applied due to the lower die thickness. Temperature was first raised to 700°C and stabilized during 5 min. Following this, the current was manually and instantly increased to its maximum until a temperature of ~1500°C was reached (within 5 to 7 seconds). Temperature was monitored with a pyrometer focused on the external surface of the die. Then the power was manually stopped, enabling natural cool down to room temperature. Classic SPS experiments were performed under 100 MPa for dwell time of 3 min at temperatures ranging from 900°C to 1300°C every 50°C. After sintering, all specimens were annealed at 800°C to remove the graphite foil and enable re-oxidation of the 3YSZ (we assume that 3YSZ was exposed during SPS to low oxygen partial pressure hence possible formation of oxygen vacancies). Eight different specimens were prepared with a maximum sintering temperature ranging from 1515°C to 1710°C.

X-ray diffraction (XRD) analyses were performed on specimens using a Bruker D4 Endeavor diffractometer with Cu-Kα wavelengths in a Bragg-Brentano geometry in the range $20° < 2\theta < 70°$. Pellets microstructures were examined at the fractured specimen surfaces with a field-emission-gun scanning electron microscope (FESEM, JEOL JEM 7800F) using 5 kV

acceleration voltage at working distance of 6 mm. All images were recorded from secondary electrons on Pt sputtered specimens (≈ 2 nm thickness). SEM images were used to determine grain sizes of all specimens, measuring the minimum of 100 grains in different locations of the specimen, and applying the intercept method with a 1.56 correction factor [17]. Densities for all specimens were determined by geometric measurements and weighing. Vickers hardness values on polished surfaces were determined using a Vickers Hardness Testing Machine (Mituyo HM200) applying 1 kg for a 10 s period. Ten measurements per specimen were performed to obtain an averaged value. High Resolution Transmission Electron Microscopy (HR-TEM) was performed on a FSPS specimen sintered at 1535°C using a JEOL JEM-2100F at 200 kV acceleration voltage available at the *Centre de Microcaractérisation Raimond Castaing*, University of Toulouse. The TEM specimen was prepared using an FEI Helios 600i focused ion beam (FIB) system.

The Electrical Impedance Spectroscopy measurements were performed in air using a Frequency Response Analyzer Autolab PGSTAT302 at 100 mV in the 10-10^6 Hz frequency range. ZView software was used for data fitting where equivalent circuit consists of two R-CPE (Resistor-Constant Phase Element) in series. The electric contacts were made using Pt grids as current collector and a Pt sputtered layer on specimen polished faces.

3. Results and discussion

3.1. Sintering profile

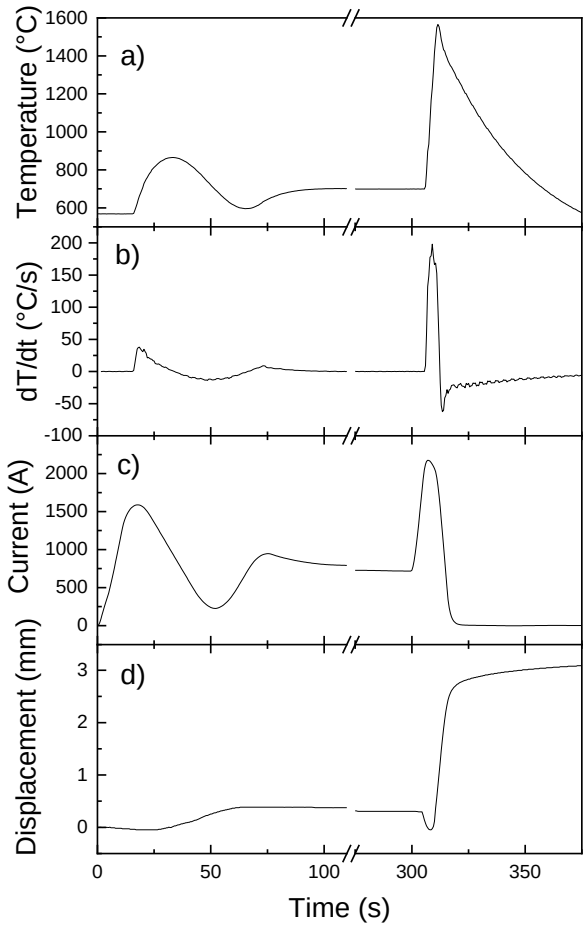

Figure 1: Experimental parameters profile during FSPS: a) temperature, b) heating rate, c) electric current and d) displacement of 3YSZ specimen sintered by FSPS at 1565°C

The temperature, heating rate, electric power, and displacement profiles versus time during heating and at the FSPS temperature of 1565°C are shown in Figure 1. As depicted in Figure 1a, the temperature increases extremely fast, from 700°C to 1565°C in less than 5 seconds. Differential temperature profile (Figure 1b) shows a maximal heating rate of 200°C/s and an average heating rate of 144°C/s over the total heating stage (less than 5 s).

As recorded in Figure 1c, although simultaneously increased around 300 s, the current is not delivered immediately, as it takes 7 seconds to reach its maximum value of 2.7 kA, and is released during 10 seconds. This process is accompanied with a strong displacement (≈ 3 mm as shown in Figure 1d) which is ascribed to the densification of the specimen. After the die

temperature of 1565°C is reached, natural cooling occurs to bring back the specimen below 700°C within tens of seconds (less than a minute). As in the case of B_4C [14], 3YSZ specimen is a NTC (negative temperature coefficient) ionic conductor in specific conditions, which is electrically insulating at room temperature and becomes more conductive as the temperature increases. This increase in conductivity enables current flow through the specimen [7], and in turn a thermal runaway hence accelerating thermal ramp as temperature increases. The overall FSPS experiment last less than 10 min, while the actual densification step lasts a few seconds only.

Some attention should be paid to the temperature measurement. Since in our FSPS device, the temperature is measured with a pyrometer focused on the outside wall of the die, some thermal gradients between the specimen's core and the external part of the die can be expected. Since the specimen becomes more conductive as the temperature increases, its temperature must be higher than the one measured on the die surface, where heat loss by radiation becomes important. This phenomenon, also valid for classical SPS experiments, is more important in FSPS due to the higher heating rates and higher current densities. Proper assessing of the temperature presents a technical challenge, also present in Flash Sintering experiments [18], and is beyond the scope of the present work. Thus, temperature measurement must be considered as valid for relative comparisons between different specimens but may not reflect the actual specimen temperatures.

3.2. XRD phase analysis

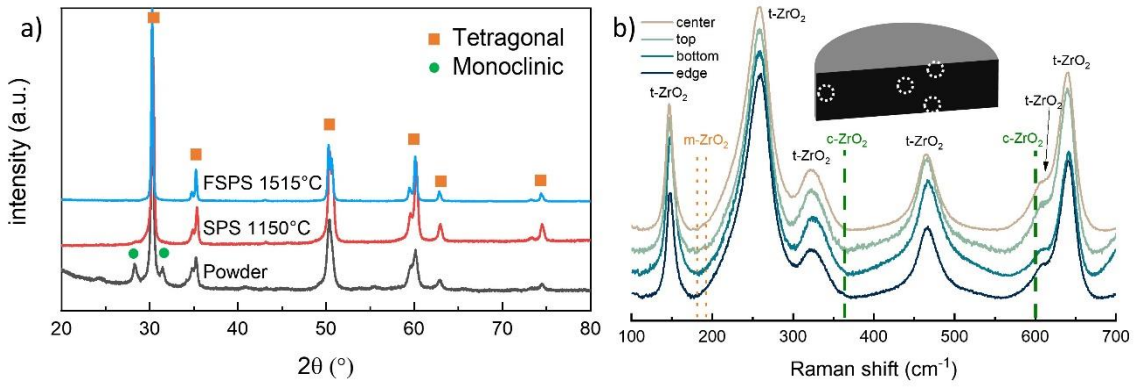

Figure 2: a) XRD patterns of as-received powder and sintered specimens (measured on specimen surfaces) and b) focused Raman spectra of FSPS sample sintered at 1620°C measured from various regions of the specimen cross section (dotted circles). m-ZrO_2, t-ZrO_2 and c-ZrO_2 stand for monoclinic, tetragonal and cubic phases of zirconia.

Sintered specimens from SPS and FSPS experiments were annealed at 800°C for 4 h and characterized by XRD to control the preservation of the tetragonal phase. As shown in Figure 2a, the as-received starting powder is composed of mixed tetragonal and monoclinic phases. After sintering and densification, pure tetragonal phase is obtained, with no significant difference between the two sintering processes. For all sintered specimens, no phase differences were observed.

Moreover, the specimen's structure homogeneity was evaluated using Raman spectroscopy. Four different regions were probed at different locations at the specimen's cross-section (top, center, bottom and edge). The similar spectra presented on Figure 2b for the specimen sintered at 1620°C confirm the homogeneity over the whole cross section. The observed bands are characteristic of tetragonal zirconia phase [19], such as expected for 3YSZ and also observed in XRD, and confirm the absence of monoclinic phase (the bands at 180 and 192 cm^{-1} relative to the monoclinic phase are not observed). Moreover, the cubic phase is characterized by a shift of Zr-O stretching band from ~640 cm^{-1} in tetragonal phase down to ~600 cm^{-1} in cubic phase

[19]. In the present case, no peak shifts appeared on the various Raman spectra, confirming the unique presence of the tetragonal phase.

3.3. Microstructure characterization SEM

SEM observations from the FSPS specimen's fracture surfaces are displayed in Figure 4. In all specimens faceted grains were observed together with neck formation and porosity between the grains. For the experiments performed at high temperatures, one may expect exaggerated grain growth. However, all specimens exhibited grain sizes below 400 nm in average, with a relatively narrow size distribution, which is most probably due to the very short sintering time of FSFS.

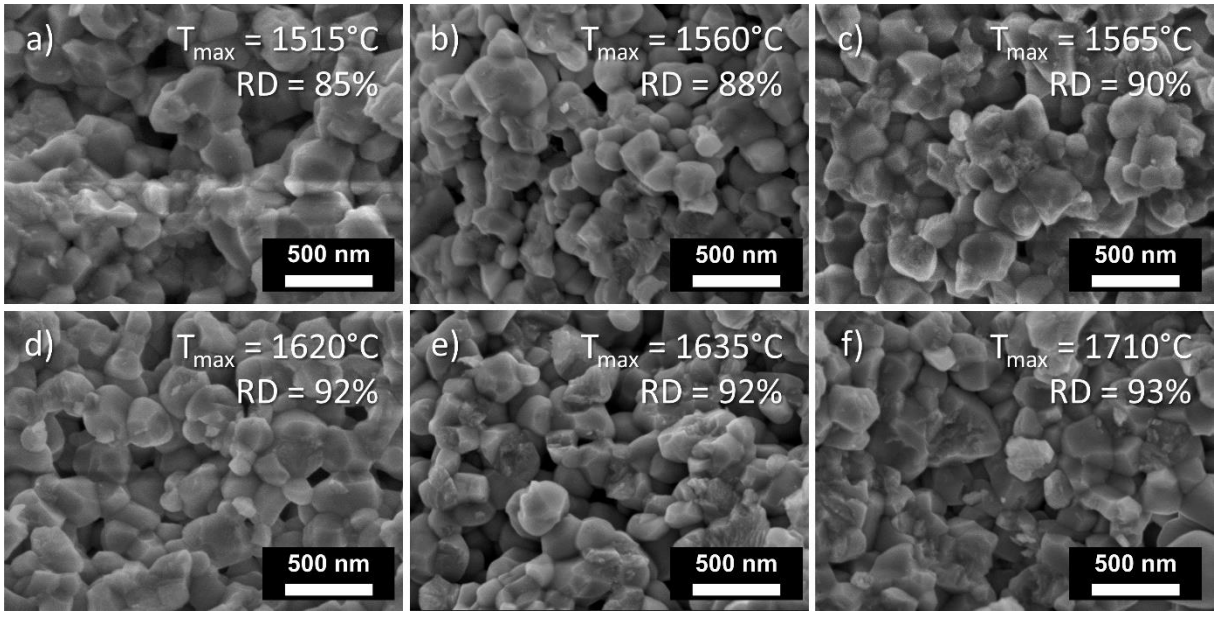

Figure 3: SEM images of 3YSZ specimens FSPS sintered at different temperatures: a) 1515°C, b) 1560°C, c) 1565°C, d) 1620°C, e) 1635°C and f) 1710°C, along with corresponding specimens relative densities.

In addition, the microstructure homogeneity was probed on the fractured specimens at different locations at the cross-section, as shown in Figure 4. Interestingly, the microstructure was very homogeneous over the specimen's fracture area, providing a great advantage compared to regular Flash Sintering technique that often leads to anisotropic microstructures

and hot spots [7]. This may be assigned to the uniaxial pressure applied on the specimen that allows to maintain good electrical and mechanical contacts over the whole surface of the specimen. Electric current must then homogeneously flow through the specimen, resulting in a properly distributed heat and temperature increase.

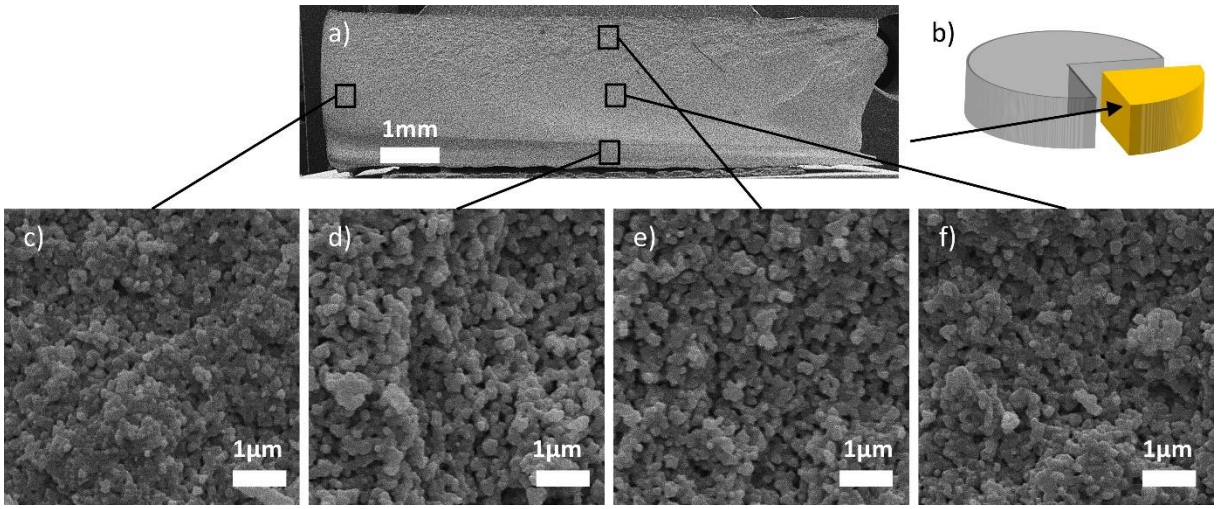

Figure 4: SEM images from the FSPS specimen sintered at 1620°C. a) low magnification, b) representation of specimen fracture prepared for observation, c) edge zone view, d) bottom, e) top and f) center. The homogeneous density and grain size at different loci are visible.

3.4. Sintering trajectory

The grain sizes measured from the SEM image analyses were plotted versus specimen relative densities to evaluate their sintering trajectory in the sintering of 3YSZ as shown in Figure 5a. Our data on the SPSed specimens are in agreement to those obtained by Flaureau et al [20], as well as data from previous studies of Bernard-Granger *et al.* [21] and Anselmi-Tamburini *et al.* [22] on YSZ (all were added to Figure 5a for comparison). These trajectories follow the same pattern as shown by Bernard-Granger *et al.* evidencing two distinct domains. A first domain concerns specimens below 97% relative density, for which densification occurs almost with no grain growth. In the second domain, between ~ 97 and 100% relative density,

significant grain growth occurs along with the final densification of the specimens. Our data obtained from SPS experiments (red open circles in Figure 5) follow the same pattern as those from the literature [21, 22]. It is noteworthy that the data from Anselmi-Tamburini *et al.* [22] follow the same pattern as the one obtained by Bernard-Granger et al. [21], while they deal with different Y_2O_3 compositions in YSZ (3% and 8% respectively). This tends to show that Y_2O_3 content, at least in this composition range, has small influence on the sintering trajectory, hence sintering/densification mechanism of YSZ in the nanometer particle size range subjected to classical SPS.

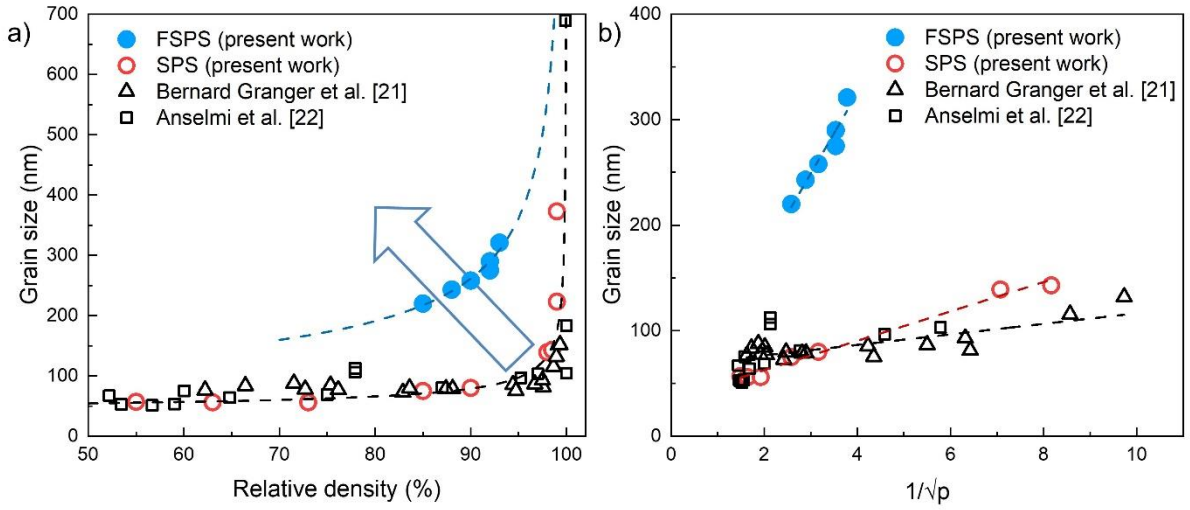

Figure 5: Sintering trajectory of nanometric 3YSZ showing the average grain size versus a) relative density and b) 1/√p (where p is the fractional porosity). The FSPS and SPS results were obtained at different conditions (ramp, dwell time, applied pressures). Dashed lines represent fitting results from FSPS and SPS data using equation (2). Current work's data are compared to literature values from [21,22]. *The arrow indicates changes in the sintering/densification mechanisms (see explanation within the text).*

On the contrary, FSPS results show significantly different behavior in the sintering trajectory as shown by the solid blue circles in Figure 5a. In this case, the results are not aligned with SPS data both from literature and from the present work (SPS data are obtained from the same starting powder). Grain growth is observed in all FSPS specimens even though they exhibit densities below 93%.

In order to describe the microstructure evolution (grain size vs. relative density), Bruch introduced a model that was applied to micron sized copper and submicronic alumina [23–25]:

$$G = \frac{\theta G_0}{\sqrt{p}} \quad (1)$$

were G and G_0 are respectively the grain size (diameter) and the initial powder particle size, p is fractional porosity (ranging from 0 to 1) and θ is a constant, assumed to be related to a geometric parameters.

This model was successfully applied to the present data, but a much better fit could be obtained by modifying the previous equation due to the smaller particle size:

$$G = \frac{\theta G_0}{\sqrt{p}} + K \quad (2)$$

Where K is a constant which is related to the initial particle size and green density. This was applied to the current dataset, along with data from Bernard-Granger *et al.* [21], in the range 50 < RD < 99% (see Figure 5b). As expected, all SPS specimens showed similar trend, although the slope is slightly different (θG_0 = 6.1 and 13.9 for data from [21] and from our present work on SPS, with similar initial particle size of 60 and 40 nm, respectively). However, a significant difference is found for FSPS specimens which exhibit θG_0 = 76.1. The resulting model obtained using equation (2) with fitted parameters are plotted in Figure 5a as dashed lines, showing a good agreement with the experimental data. To confirm the necessity to modify Burch's equation (1) to equation (2), the following information should be considered. i) the present FSPS and SPS experiments used the same 3YSZ powder, and therefore have a similar G_0 value, ii) they exhibit a different slope in the G vs. 1/√p plot (Figure 5b), i.e. describing a different θ value. Thus, θ cannot be solely affected by a geometric constant. Considering our results, this difference may be ascribed to the sintering mechanism, as further discussed below.

The grain size (G) versus relative density (RD) plots are very common in the ceramic sintering science, where the trajectory of the curve reveals the competition between two major thermal processes, i.e. particle coarsening versus densification [26]. Sintering conditions that promote surface diffusion and evaporation-condensation mechanisms are favorable for particle coarsening, and yield almost linear G-RD dependence that ends at low RD values with extremely high values of θG_0. Sintering conditions that promote grain boundary and bulk diffusions, are favorable for densification of the powder compact, and yield linear G-RD dependence that ends around 92% RD with extremely low values of θG_0. Therefore, the large arrow in Figure 5a indicates the changes in the active diffusion mechanisms during sintering, starting from bulk diffusion at the bottom right, then interface/grain boundary diffusion at the diagram's center, and ending by surface diffusion at the top left of the diagram. In this respect, while the overall SPS data (present data and those from ref. [21] and [22]) exhibit densification controlled by bulk diffusion [20], the FSPS data resemble sintering/densification mechanisms also assisted by diffusion at surfaces and interfaces.

Thus, according to equation (1), when RD $\rightarrow$ 0, i.e. p $\rightarrow$ 1, G should correspond to θG_0. Considering that θ also depends on the sintering mechanism (as shown by FSPS data), it is necessary to introduce an additional parameter K relating to the initial stage when no grain growth is expected (< 90 % RD). However, it appears that K can be neglected for larger particles/grains (probably above 100-200 nm) and equation (1) becomes a reasonable approximation. Although empirical, this model seems to be an interesting tool to predict a microstructural correlation between grain size and relative density for a given sintering mechanism. Therefore, the evolution of θ can be related to the nature of the sintering process rather than to the initial powder particle size, as was shown above for SPS and FSPS experiments made from the same starting powder. Consequently, it turns out that the fast heating rate and short sintering time have a strong impact on the competition between

densification and grain growth regimes, so that the two may be concomitant. In classical SPS sintering experiments of 3YSZ, as shown on Figure 5a, densification occurs at lower densities, then growth is activated, as expected for slow rate diffusion mechanisms, i.e. diffusion with the bulk grains and along the grain boundaries within the particle. Because the heating rate in FSPS is extremely high, grain growth regime can be activated through surface diffusion before densification occurred, which may result in modified microstructure evolution, thus in different sintering trajectory. Nevertheless, high heating rate also leads to sintering conditions where high number density of particle surfaces are free for particle sliding under the externally applied pressure, to aid rapid densification. We assume that such free surfaces are either absent or partially sintered during the heating via the classical SPS route. Therefore, the residual porosity during SPS is located at the grain boundaries, assisting densification by volume and grain boundary diffusion and as well inhibits grain growth. On the other hand, such porosities are absent at the grain boundaries during FSPS, most probably due to particle sliding and rapid surface and interfacial diffusions hence enhanced grain growth. To check the influence of such microstructural change (due to the high heating rates) on the properties, some hardness tests were performed on the specimens.

3.5. Hardness tests

The Vickers hardness (HV) of the FSPS sintered specimens were presented in Figure 6, and compared to the literature data from Muroi *et al.* [27], Luo & Stevens [28] and Fregeac et al. [29].

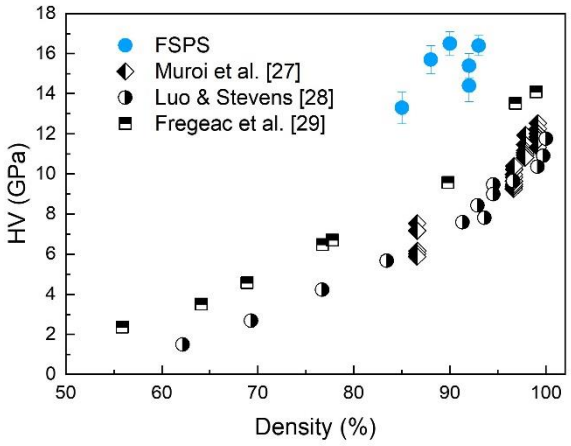

Figure 6: Vickers hardness of FSPS specimens compared to literature data, [27–29]. The error bars present the standard deviation of 10 measurements per specimen.

The Vickers hardness exhibited higher values for FSPS specimens relative to the reported literature data for 3YSZ with equivalent porosities. The same HV evolution with density was observed in zirconia with higher Y_2O_3 contents, i.e. 6 and 8 mol.% in YSZ [29,30]. In the present case, the FSPS specimen exhibited hardness values above the typical data obtained for a dense specimen, although FSPS specimens contain 5-15 vol.% porosity. The difference between our HV results for the FSPS specimens and the literature data for SPS specimens, is relatively high (almost doubled HV values) and may also be due to the load effects (i.e. 1 kg vs. 50 kg). It can be assumed that the improved hardness of FSPS specimens arises from an improved 'quality' of the grain boundaries after sintering compared to SPSed specimens. To get more insight about the 'quality' of these grain boundaries, TEM observations and electrical measurements were carried out on the FSPS specimens.

3.6. Local microstructure observation

To better understand the hardness results, local microstructure observations were performed. HR-TEM images from the FSPS specimens revealed grains with faceted grain boundaries, as displayed in Figure 7. Figure 7a.1) shows the typical microstructure of the grains, the inter-

grain porosity and a triple junction. A magnified view is shown in Figure 7a.2), highlighting the triple junction with no porosity. Figure 7a.3) shows the lattice imaging of the grain boundary region assigned by rectangle in Figure 7a.2).

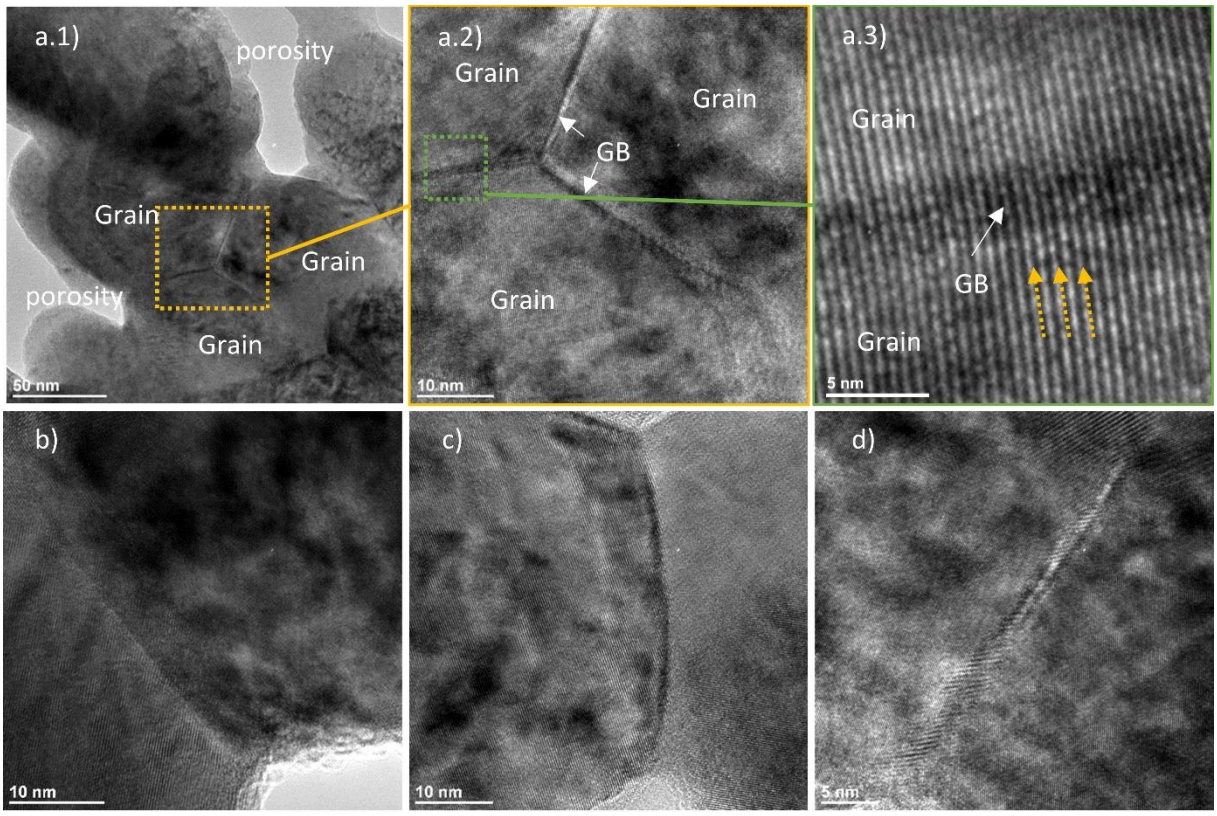

Figure 7: HRTEM images from different locations of FSPS specimen sintered at 1535°C. a.1) to a.3) correspond to different magnifications of the same area, while b), c) and d) correspond to other regions in the specimen. Arrows indicate grain boundaries (GB) and dotted arrows highlight the atomic rows through GB interface on a.3).

As observed in the low magnification view in Figure 7a.1), a surprising feature of this specimen deals with the contrast between large inter-grain porosities and a triple junction showing no residual porosity. The magnified view in Figure 7a.2) confirms this observation with nicely uniform grain boundaries (GB) and the absence of small residual porosity at the triple junctions. The residual porosity (5 to 15 vol.%) is large and its average size is comparable to the grain size. This observation suggests that sintering went through its final stage in such

junctions, while large open or closed pores observed between the grains (see SEM images in Figure 3), necessitate much longer process durations towards full densification. In Figure 7a.3), we focused the observations at the GB area. The magnified image shows (highlighted by dotted arrows) atomic rows coherently crossing the GB interface. This highlights the high crystalline quality of the grains at their GB, with extremely thin GB width, that may resemble epitaxial GB interface, or low angle grain boundaries. Observations of several other zones in the specimen, as shown in Figure 7b), c) and d), confirmed the low GB thickness. Such grain boundaries are characteristics of the hot-pressed or isostatically hot pressed 3YSZ with superior mechanical properties [31]. The present crystalline GBs are consistent with the high hardness of the porous FSPS specimens.

To confirm the GB 'quality', and step from local observation to macroscopic quantification, Electrical Impedance Spectroscopy measurements were performed on FSPS and SPS specimens.

3.7. Electrical impedance measurements

Electrical Impedance Spectroscopy (EIS) measurements were performed on SPS specimen sintered at 1250°C with RD of 99.5%, average grain size G = 220 nm and FSPS specimen sintered at 1620°C with RD of 90% and G = 225 nm. Therefore, albeit their different densities, their grain sizes are similar, hence enable comparison. Two main contributions were observed in the form of Debye-like relaxation, which are assigned to the grain (higher frequency) and the grain boundary (lower frequency) contributions (Figure 8). Both were modeled using equivalent circuit method. Each one of them are associated to an equivalent circuit made of a resistor, representing either bulk or grain boundary resistance (R_{bulk} and R_{GB}) and a constant phase element (CPE) [32], connected in parallel as displayed in the inset of Figure 8. Typical

impedance diagrams recorded at 300°C under air are reported in Figure 8. To better visualize the impedance ratio of bulk to GB for both SPS and FSPS specimens, the data was plotted as Z'/R_{bulk} and Z''/R_{bulk}. First, one can observe that GB contribution to the impedance is proportionally twice than the bulk (grain) contribution in the case of SPS as compared to the FSPS specimens at 300°C. This indicates that despite the lower specimen density, the GB's in the FSPS specimen exhibit higher conductivity than in the SPS specimen.

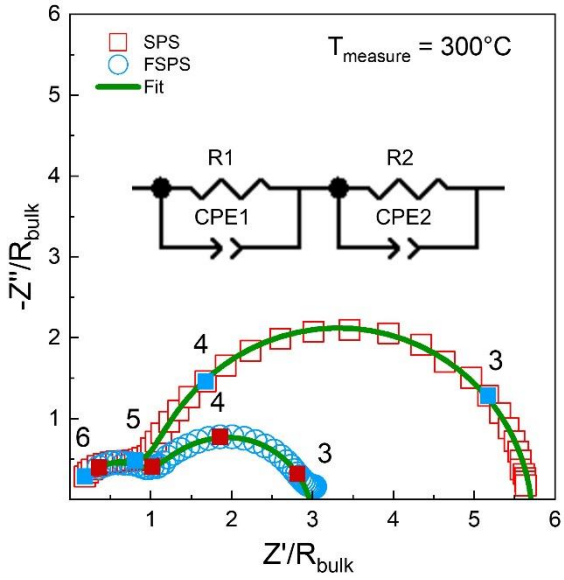

Figure 8: Nyquist plot of electrical impedance of FSPS (1620°C) and SPS (1250°C) performed at 300°C and their respective fitting curves using the equivalent circuit. The axes were normalized to the fitted grain resistance (R_{bulk}). The logarithm of frequencies are displayed for both plots.

Fitting the obtained values allowed to evaluate the conductivity (σ_i), capacitance (C_i), and relaxation frequency (f_{0i}), with i denoting either bulk or grain boundary. The overall results are plotted in Figure 9 for temperatures ranging between 200 and 400°C in Arrhenius-like plots. Temperature dependence of the conductivity is plotted in Figure 9a. In both bulk and GB, the difference between SPS and FSPS specimen is more visible at lower temperatures and tends to be reduced when temperature increases. However, FSPS conductivity is higher in both cases. As a confirmation, the conductivity difference is larger in the case of GB. Capacitance and

frequency are respectively temperature-free and geometric-free parameters and can be considered as identification parameters of the specimens. They can be used to qualify the nature of the observed contributions [33]. Here it can be noticed that capacitance data are similar for SPS and FSPS specimens, both in the case of GB and bulk. The same observation can be made from relaxation frequencies.

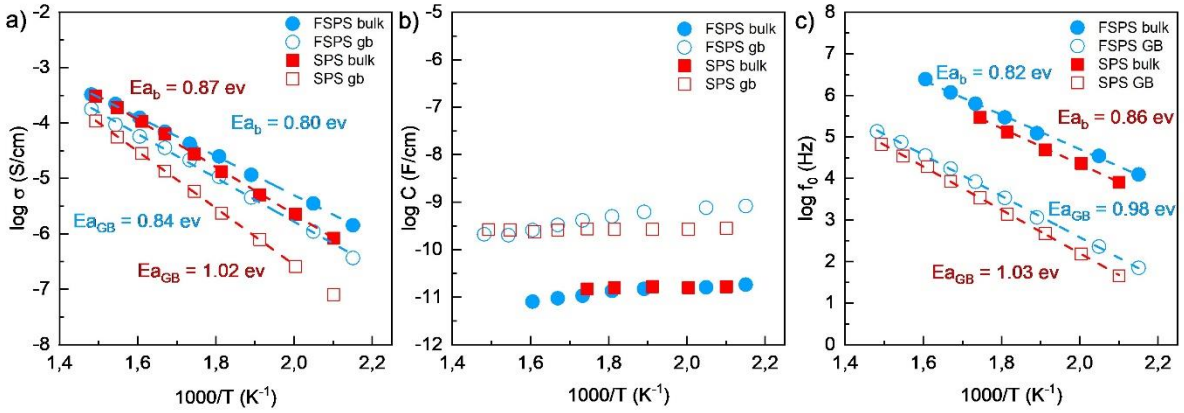

Figure 9: Data obtained from electrical impedance spectroscopy measurements fits. a) logarithm of conductivity, d) logarithm equivalent capacitance and e) logarithm of relaxation frequency. The activation energies are displayed on a) and c).

These data are close to those observed for sintered YSZ specimens [34,35] and confirm the chemical and structural nature of the electrical processes. Activation energies that depend on the line slope were calculated from the Arrhenius-like plots of frequency or conductivity for GB and bulk. The data obtained for SPS are consistent with that reported for 3YSZ after conventional sintering [36]. According to Figure 9c, we calculated the activation energy values of 0.86 eV and 1.03 eV for bulk and GB conductivity, respectively. The corresponding activation energies determined for the FSPS specimen are slightly lower with 0.82 eV and 0.98 eV, but remain in the same range of values found for ionic conductivity in YSZ densified by conventional sintering [36], as well as flash sintering [34,37].

In the case of zirconia based ceramics, impedance data can be used to evaluate the grain boundary thickness [34,35]. To this end, the fact that the apparent dielectric properties may differ from intrinsic (specific) properties were considered. These depend on geometric parameters, and especially the GB thickness (δ_{GB}) to grain size (G) ratio. In the case of bulk contributions, it can be assumed that GB thickness is negligible compared to grain size. This induces that the values of specific dielectric properties for bulk contributions can be similar to the apparent values: $\sigma_{bulk}^{sp} \cong \sigma_{bulk}^{app}$, and $\varepsilon_{bulk}^{sp} \cong \varepsilon_{bulk}^{app}$ (where σ_{bulk}^{sp} and ε_{bulk}^{sp} stand for specific bulk conductivity and specific bulk permittivity, and σ_{bulk}^{app} and ε_{bulk}^{app} stand for apparent bulk conductivity and permittivity, respectively). However, in the case of GB contributions, the δ_{GB}/G ratio must be considered. The following relations are commonly used in the literature [34,35,38]:

$$\sigma_{GB}^{sp} = \left(\frac{\delta_{GB}}{G}\right) \sigma_{GB} \tag{3}$$

$$\varepsilon_{GB}^{sp} = \left(\frac{\delta_{GB}}{G}\right) \varepsilon_{GB} \tag{4}$$

And the capacitance is defined as:

$$C_i = \varepsilon_0 \varepsilon_i \tag{5}$$

Where ε_0 is vacuum permittivity and ε_i the GB or bulk permittivity.

Moreover, in zirconia based ceramics, it can be considered that $\varepsilon_{GB}^{sp} \cong \varepsilon_{bulk}^{sp}$ [38] (with ε_{GB}^{sp} and ε_{bulk}^{sp} being the specific permittivity of grain boundaries and bulk, respectively). According to equations (4) and (5):

$$\delta_{GB} = \frac{C_{bulk}}{C_{GB}} G \tag{6}$$

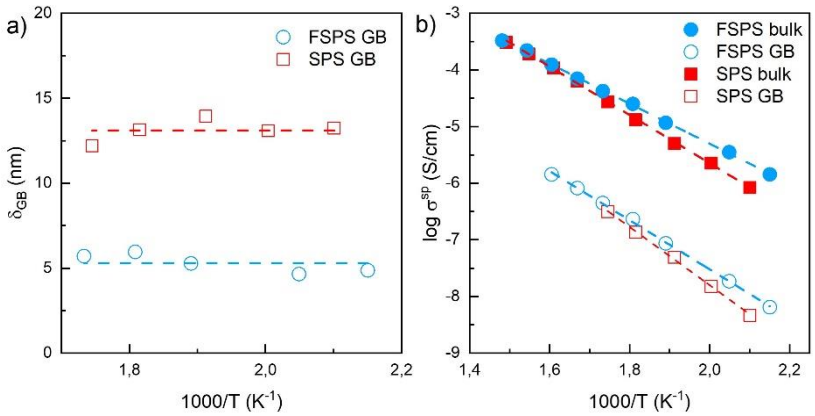

Figure 10: a) Grain boundary thickness obtained from equation (6), and b) logarithm of specific conductivity.

Resulting data of δ_{GB} at various temperatures were plotted in Figure 10a for SPS and FSPS specimens. In both cases, the GB thickness values are very stable with temperature evolution, and an average value of 13.1 nm and 5.3 nm were obtained for SPS and FSPS specimens, respectively. SPS specimen value is consistent with Bernard-Granger *et al.* data [35] for 3YSZ who reported an average value of 13 nm for δ_{GB} using similar calculation method, whatever the sintering temperature from 1050 to 1200°C (therefore independent on porosity, ranging from 0 to 24%). Thus, FSPS specimens exhibit a GB thickness 2.5 times thinner than those in the SPS specimens. This supports the previous observations made by HR-TEM. The resulting specific conductivity can then be calculated according to equation (3), and are plotted for both types of specimens in Figure 10b. Interestingly, GB specific conductivities of the two samples are almost the same (open circles and cubes in Figure 10b). Also, bulk specific conductivities of FSPS and SPS exhibit the same difference as the one observed for GBs. Thus, the two samples have the same intrinsic electrical behavior, confirming their similar GB and bulk nature (chemical and structural). The whole difference in their macroscopic (apparent) electrical behavior can be explained by their GB thickness (δ_{GB}) difference. This confirms that FSPS does not have different impact on chemical and structural nature of the initial powder, but rather strongly affect the GB thickness and most probably its mechanical strength. However, the microscopic observations confirm very high sintering efficiency at GB interfaces. This results

in better ionic conductivity even for porous FSPS specimens than almost fully-dense SPS specimens. The lower GB thickness may also be associated to changes in the sintering mechanism; nevertheless this aspect needs further investigations.

The present work highlights the impact of FSPS route on the 3YSZ microstructure and its macroscopic properties, associated with microscopic observations. This process also opens the possibility to rapidly densify materials regardless of their electric conductivity, along with a homogeneous microstructures, which is a great asset as compared to Flash Sintering. Further work will be needed to address the influence of processing parameters on the sintering mechanisms, so that various microstructures could be designed. In particular, working on pressure/time increase could be a relevant way to increase densities while preserving the submicron grain sizes.

Another focus should be paid to Yttrium segregation, which may result in phase transitions. Segregation of Y_2O_3 to surfaces and grain boundaries of tetragonal zirconia during sintering and grain growth is well documented in the zirconia literature [38]. It arises from decrease in solid solubility of Y^{+3} in YSZ with the temperature increase above 1000°C, and the two-phase cubic + monoclinic phase assemblage. Although our investigations by XRD and local Raman spectroscopy did not reveal the presence of other phases than tetragonal zirconia, a more refined local analysis are needed to confirm this aspect.

4. Conclusions

Using a conventional SPS setup with a modified die allowed to reach extremely high thermal ramp up to 200°C/s hence Flash-SPS (FSPS) which was applied to 3YSZ specimens. Within a few seconds, green nanoparticle compacts were densified by FSPS up to 93% of the theoretical density at measured temperature of 1710°C. Comparison of the sintering trajectory (densities,

porosities, and grain sizes) with our conventional SPS reference specimens as well as to the 3YSZ literature data, point out different sintering mechanisms (both densification and grain growth) as compared to conventional SPS. This is further supported by the improved hardness compared to specimens sintered by SPS to equivalent porosity levels. HRTEM observations and electrical characterization further supported this aspect and revealed the role of the GB's in ceramic properties. The enhanced hardness was related to a specific sintering mechanism that promotes GB reinforcement despite the presence of residual porosity. Apparently, the rapid heating imposes sudden temperature increase at the nanoparticle surfaces that, in turn, undergo rapid sintering and densification facilitated by the applied pressure. This opens interesting opportunities for the preparation of porous lightweight structural ceramics with improved mechanical properties.

5. References

[1] C. Manière, E. Nigito, L. Durand, A. Weibel, Y. Beynet, C. Estournès, Spark plasma sintering and complex shapes: The deformed interfaces approach, Powder Technol. 320 (2017) 340–345.

[2] Z.Y. Hu, Z.H. Zhang, X.W. Cheng, F.C. Wang, Y.F. Zhang, S.L. Li, A review of multi-physical fields induced phenomena and effects in spark plasma sintering: Fundamentals and applications, Mater. Des. 191 (2020) 108662. doi:10.1016/j.matdes.2020.108662.

[3] R. Chaim, R. Marder, C. Estournés, Z. Shen, Densification and preservation of ceramic nanocrystalline character by spark plasma sintering, Adv. Appl. Ceram. 111 (2012) 280–285. doi:10.1179/1743676111Y.0000000074.

[4] O. Guillon, J. Gonzalez-Julian, B. Dargatz, T. Kessel, G. Schierning, J. Rathel, M. Herrmann, Field-assisted sintering technology/spark plasma sintering: Mechanisms, materials, and technology developments, Adv. Eng. Mater. 16 (2014) 830–849.

[5] M. Yu, S. Grasso, R. Mckinnon, T. Saunders, M.J. Reece, Review of flash sintering: materials, mechanisms and modelling, Adv. Appl. Ceram. 116 (2017) 24–60.

[6] W. Ji, B. Parker, S. Falco, J.Y. Zhang, Z.Y. Fu, R.I. Todd, Ultra-fast firing: Effect of heating rate on sintering of 3YSZ, with and without an electric field, J. Eur. Ceram. Soc. 37 (2017) 2547–2551.

[7] M. Biesuz, V.M. Sglavo, Flash sintering of ceramics, J. Eur. Ceram. Soc. 39 (2019) 115–143. doi:10.1016/j.jeurceramsoc.2018.08.048.

[8] E.A. Olevsky, S.M. Rolfing, A.L. Maximenko, Flash (Ultra-Rapid) Spark-Plasma Sintering of Silicon Carbide, Sci. Rep. 6 (2016) 33408.

[9] C. Manière, G. Lee, E.A. Olevsky, All-Materials-Inclusive Flash Spark Plasma Sintering, Sci. Rep. 7 (2017) 1–8.

[10] S. Grasso, T. Saunders, H. Porwal, O. Cedillos-Barraza, D.D. Jayaseelan, W.E. Lee, M.J. Reece, Flash spark plasma sintering (FSPS) of pure ZrB_2, J. Am. Ceram. Soc. 97 (2014) 2405–2408. doi:10.1111/jace.13109.

[11] S. Grasso, T. Saunders, H. Porwal, B. Milsom, A. Tudball, M. Reece, Flash Spark Plasma Sintering (FSPS) of α and β SiC, J. Am. Ceram. Soc. 99 (2016) 1534–1543.

[12] R. McKinnon, S. Grasso, A. Tudball, M.J. Reece, Flash spark plasma sintering of cold-Pressed TiB_2-hBN, J. Eur. Ceram. Soc. 37 (2017) 2787–2794. doi:10.1016/j.jeurceramsoc.2017.01.029.

[13] C. Manière, G. Riquet, S. Marinel, Dielectric properties of flash spark plasma sintered $BaTiO_3$ and $CaCu_3Ti_4O_{12}$, Scr. Mater. 173 (2019) 41–45. doi:10.1016/j.scriptamat.2019.07.048.

[14] B. Niu, F. Zhang, J. Zhang, W. Ji, W. Wang, Z. Fu, Ultra-fast densification of boron carbide by flash spark plasma sintering, Scr. Mater. 116 (2016) 127–130. doi:10.1016/j.scriptamat.2016.02.012.

[15] O. Vasylkiv, H. Borodianska, Y. Sakka, D. Demirskyi, Flash spark plasma sintering of ultrafine yttria-stabilized zirconia ceramics, Scr. Mater. 121 (2016) 32–36. doi:10.1016/j.scriptamat.2016.04.031.

[16] M. Biesuz, R. Sedlák, T. Saunders, A. Kovalčíková, J. Dusza, M. Reece, D. Zhu, C. Hu, S. Grasso, Flash spark plasma sintering of 3YSZ, J. Eur. Ceram. Soc. 39 (2019) 1932–1937. doi:10.1016/j.jeurceramsoc.2019.01.017.

[17] M.I. Mendelson, Average Grain Size in Polycrystalline Ceramics, J. Am. Ceram. Soc. 52 (1969) 443–446. doi:10.1111/j.1151-2916.1969.tb11975.x.

[18] J.M. Lebrun, C.S. Hellberg, S.K. Jha, W. Kriven, A. Steveson, K.C. Seymour, N. Bernstein, C. Erwin, R. Raj, In-situ Measurements of Lattice Expansion Related to Defect Generation During Flash Sintering, J. Am. Ceram. Soc. 100 (2017) 4965–4970.

[19] Y. Hemberger, N. Wichtner, C. Berthold, K.G. Nickel, Quantification of yttria in stabilized zirconia by Raman spectroscopy, Int. J. Appl. Ceram. Technol. 13 (2016) 116–124. doi:10.1111/ijac.12434.

[20] A. Flaureau, A. Weibel, G. Chevallier, C. Estournès, Study of the densification and grain growth mechanisms occurring during spark plasma sintering of different submicronic yttria-stabilized zirconia powders, J. Eur. Ceram. Soc. 41 (2021) 3581–3594. doi:10.1016/j.jeurceramsoc.2021.01.032.

[21] G. Bernard-Granger, C. Guizard, N. Monchalin, Étude du frittage SPS d'une poudre de zircone ultrafine, Matériaux Tech. 95 (2007) 235–239. doi:10.1051/mattech:2008007.

[22] U. Anselmi-Tamburini, J.E. Garay, Z.A. Munir, A. Tacca, F. Maglia, G. Spinolo, Spark plasma sintering and characterization of bulk nanostructured fully stabilized zirconia: Part I. Densification studies, J. Mater. Res. 19 (2004) 3255–3262. doi:10.1557/JMR.2004.0423.

[23] C.A. Bruch, Sintering kinetics for high density alumina process, Am. Ceram. Soc. Bull. 41 (1962) 799–806.

[24] H.Y. Suzuki, K. Shinozaki, M. Murai, H. Kuroki, Quantitative Analysis of Microstructure Development during Sintering of High Purity Alumina made by high-speed centrifugal compaction process, J. Japan Soc. Powder Powder Metall. 45 (1998) 1122–1130.

[25] R.M. German, Sintering: from empirical observations to scientific principles, Elsevier, 2014.

[26] M. Barsoum, Fundamentals of ceramics, 2019.

[27] M. Muroi, G. Trotter, P.G. McCormick, M. Kawahara, M. Tokita, Preparation of nano-grained zirconia ceramics by low-temperature, low-pressure spark plasma sintering, J. Mater. Sci. 43 (2008) 6376–6384. doi:10.1007/s10853-008-2559-4.

[28] J. Luo, R. Stevens, Porosity-dependence of elastic moduli and hardness of 3Y-TZP ceramics, Ceram. Int. 25 (1999) 281–286. doi:10.1016/S0272-8842(98)00037-6.

[29] A. Fregeac, F. Ansart, S. Selezneff, C. Estournès, Relationship between mechanical properties and microstructure of yttria stabilized zirconia ceramics densified by spark plasma sintering, Ceram. Int. 45 (2019) 23740–23749. doi:10.1016/j.ceramint.2019.08.090.

[30] U. Anselmi-Tamburini, J.E. Garay, Z.A. Munir, A. Tacca, F. Maglia, G. Spinolo, Spark plasma sintering and characterization of bulk nanostructured fully stabilized zirconia: Part II. Characterization studies, J. Mater. Res. 19 (2004) 3263–3269. doi:10.1557/JMR.2004.0423.

[31] F. Wakai, S. Sakaguchi, Y. Matsuno, Superplasticity of Yttria-Stabilized Tetragonal ZrO_2 polycrystals, Adv. Ceram. Mater. 1 (1986) 259–263.

[32] E. Barsoukov, J.R. Macdonald, Impedance Spectroscopy Theory, Experiment, and Applications, Wiley, 2005.

[33] J.T.S. Irvine, D.C. Sinclair, A.R. West, Electroceramics: Characterization by Impedance Spectroscopy, Adv. Mater. 2 (1990) 132–138. doi:10.1002/adma.19900020304.

[34] J.C. M'Peko, J.S.C. Francis, R. Raj, Impedance spectroscopy and dielectric properties of flash versus conventionally sintered yttria-doped zirconia electroceramics viewed at the microstructural level, J. Am. Ceram. Soc. 96 (2013) 3760–3767. doi:10.1111/jace.12567.

[35] G. Bernard-Granger, C. Guizard, S. Surblé, G. Baldinozzi, A. Addad, Spark plasma sintering of a commercially available granulated zirconia powder-II. Microstructure after sintering and ionic conductivity, Acta Mater. 56 (2008) 4658–4672. doi:10.1016/j.actamat.2008.05.031.

[36] M.C. Steil, F. Thevenot, M. Kleitz, Densification of Yttria-Stabilized Zirconia : Impedance Spectroscopy Analysis, J. Electrochem. Soc. 144 (1997) 390–398.

[37] K.H. Christian, H. Charalambous, S.K. Jha, T. Tsakalakos, Current-ramp assisted sintering of 3YSZ: Electrochemical and microstructural comparison to flash and thermal sintering, J. Eur. Ceram. Soc. 40 (2020) 436–443. doi:10.1016/j.jeurceramsoc.2019.09.036.

[38] X. Guo, J. Maier, Grain Boundary Blocking Effect in Zirconia: A Schottky Barrier Analysis, Electrochem. Soc. 148 (2001) E121.